RSC Advances

PAPER

View Article Online
View Journal | View Issue



Cite this: *RSC Adv.*, 2023, **13**, 23638

# Noble metal-free ternary cobalt–nickel phosphides for enhanced photocatalytic dye-sensitized hydrogen evolution and catalytic mechanism investigation†

Zhixing Cheng,[ab] Yiqin Xu[a] and Bin Fei*[b]

Transition metal phosphides have emerged as compelling alternatives to noble metal catalysts for photocatalytic hydrogen evolution, owing to their high efficiency, stability, ease of preparation, and low-cost-effectiveness. This study investigates a series of binary and ternary phosphides predominantly composed of cobalt and nickel employed for photocatalytic dye-sensitized hydrogen evolution. Under the optimal dye-to-catalyst mass ratio, CoNiP exhibited the highest hydrogen evolution activity (12.96 mmol $g^{-1}$ $h^{-1}$), demonstrating more significant and satisfactory performance than a variety of other reported materials. This can be attributed to the high conductivity and low hydrogen evolution overpotential of phosphides, which result from their metallic characteristics and the presence of free electrons, which promote efficient electron transfer between the catalyst and sensitizer. Density functional theory calculations revealed that the cobalt incorporation into the binary phosphides causes a negative shift in the average d-band center for CoNiP, weakening the adsorption affinity of the catalyst towards $H_2$ molecules, thus effectively improving the hydrogen evolution rate compared to the pure binary phosphides. This work provides valuable insights for the development of low-cost and high-performance ternary phosphide photocatalysts.

Received 24th June 2023
Accepted 19th July 2023

DOI: 10.1039/d3ra04235a

rsc.li/rsc-advances



## Introduction

The global energy crisis poses a significant and urgent challenge for human society, underscoring the need to explore sustainable energy sources.[1,2] Hydrogen production, particularly through photocatalysis, emerges as a promising solution, given the abundant availability of solar energy as a renewable and environmentally friendly resource.[3–5] The pioneering work by Fujishima *et al.* in 1972, demonstrating photoelectrochemical water splitting on a rutile titanium dioxide ($TiO_2$) anode, paved the way for photocatalytic water splitting using semiconductor photocatalysts for $H_2$ evolution.[6–8] Since then, extensive research has been conducted on various semiconductor materials for their potential application in photocatalytic reactions, such as cadmium sulfide (CdS),[9] cadmium selenide (CdSe),[10] strontium titanate ($SrTiO_3$),[11] zinc oxide (ZnO),[12] g-$C_3N_4$,[13] silver phosphate ($Ag_3PO_4$)[14] *etc.* Even the traditional semiconductors, including $TiO_2$, can be modified by defect engineering and promoted by magnetic field effect to achieve a higher photocatalytic performance.[15,16] In addition to the sole use of semiconductors as a photocatalyst, the combination of two types of semiconductors to form Z-scheme heterojunction, which can promote efficient charge separation and transfer, has also become a hot research field.[17,18] However, a common and immanent limitation observed in most catalytic semiconductors is their wide band gap, which restricts their light absorption primarily to ultraviolet wavelengths, thereby resulting in low solar energy utilization efficiency.[19–21]

In order to enhance the visible light absorption capacity of photocatalytic systems, an effective and straightforward approach is the utilization of organic dye sensitization.[22,23] Among such dyes, Eosin-Y (EY) has been extensively studied and proven to exhibit exceptional sensitizing properties for photocatalytic hydrogen evolution.[24] In a dye-sensitized photocatalytic hydrogen evolution reaction (HER) system, the presence of an efficient HER cocatalyst is essential to minimize overpotential, facilitate the separation of photogenerated electrons and holes, and enhance the overall efficiency of the photocatalytic HER process.[25–27] Noble metals, including platinum (Pt),[28] ruthenium (Ru),[29] rhodium (Rh),[30] gold (Au)[31] and palladium (Pd),[32] have demonstrated remarkable catalytic properties as cocatalysts.[33] However, their widespread industrial

[a]*Institute of Semiconductors, Guangdong Academy of Sciences, Guangzhou 510070, P. R. China. E-mail: zhixing.cheng@polyu.edu.hk*

[b]*School of Fashion & Textiles, The Hong Kong Polytechnic University, Hong Kong 100872, P. R. China. E-mail: bin.fei@polyu.edu.hk*

† Electronic supplementary information (ESI) available: Experimental section (electrochemical measurements and computational methodology) and characterization (synthesis flows, XRD, SEM, TEM, mapping, EDX, XPS). See DOI: https://doi.org/10.1039/d3ra04235a

implementation is hindered by cost considerations and challenges associated with post-reaction recovery.[34] Consequently, non-noble metal composites have emerged as highly promising alternatives to noble metal cocatalysts.

Transition metal oxides,[35,36] nitrides,[37,38] hydroxides,[39,40] sulfides,[4,41,42] carbides,[43,44] and phosphide[45,46] have been extensively studied as potential cocatalysts in photocatalytic systems.[47] Among these materials, transition metal phosphides have gained significant attention due to their remarkable efficiency and cost-effectiveness.[48] Furthermore, studies have indicated that the structure and electron distribution of transition metal phosphides exhibits similarities to hydrogenated enzymes, suggesting a higher propensity for the formation of active sites.[49] Notably, the presence of phosphorus (P) in transition metal phosphides contributes to higher electronegativity and increased affinity towards protons, facilitating the participation of more $H^+$ ions in the hydrogen evolution reaction and thus accelerating the rate of hydrogen evolution.[50] Specifically, among various transition metal phosphides, $NiP_2$ has demonstrated favorable catalytic activity owing to its unique structural advantages.[51] The incorporation of phosphorus atoms into nickel phosphide results in longer bonds between Ni atoms compared to the face-centered cubic structure, while the bond length between Ni and P atoms becomes shorter, resulting in a denser crystal structure. This arrangement creates a synergistic effect between exposed P and Ni atoms on the surface, leading to the presence of numerous proton and hydrogen molecule adsorption sites on the nickel phosphide surface.[52] Similarly, CoP has attracted considerable attention due to its resemblance to zero-valent metals like platinum (Pt), as well as its exceptional electrochemical HER performance and superior stability in both acidic and alkaline media.[53]

Nonetheless, single-component phosphides suffer from drawbacks such as insufficient electrical conductivity and poor stability, which restrict their practical application.[49] Inspired by the enhanced electrochemical activity achieved through metal doping in metal oxides and sulfides, the investigation of ternary metal phosphides containing two distinct metal cations offers the potential for attaining state-of-the-art performance in photocatalytic water splitting.[54] While the utilization of CoP and $Ni_2P$ as cocatalysts in photocatalytic HER has been reported,[55,56] the exploration of ternary phosphides comprising varying ratios of Co and Ni as catalysts in dye-sensitized HER systems remains relatively unexplored.

In this study, a series of binary and ternary phosphides containing cobalt and nickel were successfully synthesized and employed for photocatalytic dye-sensitized hydrogen evolution. Specifically, two ternary phosphides with cobalt–nickel ratios of 1 : 1 and 1 : 3 and two binary phosphides (CoP and $Ni_2P$) were investigated. The catalytic hydrogen evolution activity was found to be closely related to the chemical composition of the catalysts, with CoNiP exhibiting the highest performance, while the ternary phosphides outperformed the binary phosphides in terms of activity. Under the optimal conditions with the best ratio of dye to catalyst mass, CoNiP achieved a hydrogen evolution activity of 12.96 mmol $g^{-1}$ $h^{-1}$. Electrochemical characterization further confirmed the superior properties of CoNiP, including high electron capacity, conductivity, and low hydrogen evolution overpotential. Density functional theory (DFT) calculations revealed that the introduction of cobalt into phosphides can alter the position of the d-band center, thereby reducing the adsorption affinity towards $H_2$ molecules and enhancing the photocatalytic hydrogen evolution in the light-driven reaction. Consequently, the ternary phosphide CoNiP exhibited higher hydrogen evolution efficiency compared to the binary phosphides.

## Experimental section

### Reagents

All chemicals are of analytical grade and are obtained from commercial suppliers and used without further purification. Cobalt(II) nitrate hexahydrate ($Co(NO_3)_2 \cdot 6H_2O$, 98%), nickel(II) chloride hexahydrate ($NiCl_2 \cdot 6H_2O$, 98%) and sodium hypophosphite monohydrate ($NaH_2PO_2 \cdot H_2O$, AR) are purchased from Alfa Aesar, Ltd. Triethanolamine (TEOA, $C_6H_{15}NO_3$, AR) is purchased from Aladdin Chemical Co., Ltd. Eosin-Y disodium salt ($C_{20}H_6Br_4Na_2O_5$, RG) is purchased from Adamas Reagent, Ltd.

### Synthesis of photocatalysts

**Synthesis of cobalt phosphide (CoP).** The synthesis of CoP involved the controlled reaction of $Co(NO_3)_2 \cdot 6H_2O$ and $NaH_2PO_2 \cdot H_2O$ with a mole ratio of 1 : 5. The precursors (0.291 g of $Co(NO_3)_2 \cdot 6H_2O$ and 0.63 g $NaH_2PO_2 \cdot H_2O$) were dissolved in 10 mL of deionized water. The solution was stirred and subjected to ultrasonic treatment for 30 min. Then it was subsequently dried in an oven to obtain some powder precursor. The obtained precursor was then loaded into a quartz boat and placed inside a tubular furnace, and the air in the furnace tube was purged with inert $N_2$ gas after adding the sample. The furnace was heated to 300 °C at a temperature raising rate of 2 °C $min^{-1}$ and maintained at the reaction temperature for 1 hour. The resulting product was thoroughly washed with water and alcohol twice, followed by centrifugation, drying and collection.

**Synthesis of nickel phosphide ($Ni_2P$).** The synthesis procedure for $Ni_2P$ was similar to that of CoP, with the exception of the reactant selection. $NiCl_2 \cdot 6H_2O$ (0.238 g) was used instead of $Co(NO_3)_2 \cdot 6H_2O$, while the remaining steps remained unchanged. The heating conditions involved heating the precursor to 220 °C at a rate of 5 °C $min^{-1}$ and maintaining this temperature for 1 hour. The resulting product was subjected to water and alcohol washing, centrifugation, drying, and collection.

**Synthesis of cobalt–nickel phosphide with different metal ratios.** To investigate the influence of metal ratios on the properties of cobalt–nickel phosphide, the reactant ratios of cobalt and nickel metal salts were varied as 1 : 1 and 1 : 3. For the CoNiP sample, we put 0.291 g of $Co(NO_3)_2 \cdot 6H_2O$, 0.238 g of $NiCl_2 \cdot 6H_2O$ and 1.26 g of $NaH_2PO_2 \cdot H_2O$ as precursors. For the $CoNi_3P$ sample, we put 0.145 g of $Co(NO_3)_2 \cdot 6H_2O$, 0.357 g of $NiCl_2 \cdot 6H_2O$ and 1.26 g of $NaH_2PO_2 \cdot H_2O$ as precursor. The synthesis procedure described above was followed, with the

heating conditions adjusted to 250 °C at a rate of 5 °C $min^{-1}$ for 1 hour. The resulting products were subjected to the same post-synthesis treatments as mentioned earlier.

### Characterization

X-ray powder diffraction (XRD) measurements are performed using a powder X-ray diffractometer (Rigaku Miniflex 600) with Cu Kα radiation ($\lambda = 1.54178$ Å). The $2\theta$ range is set from 5° to 80° and the measurement rates are kept at 5° $min^{-1}$. The morphological structure and microstructures of the samples are characterized using scanning electron microscopy (SEM) (FE-SEM, Hitachi S4800, Japan) and transmission electron microscopy (TEM) (JEOL model JEM 2100 EX instrument) measurements. In addition, high-resolution TEM, selected area electron diffraction (SAED) and elemental mapping measurements are also performed using the same TEM instrument. X-ray photoelectron spectroscopy (XPS) is collected using an AXIS Ultra DLD (Shimadzu, Japan) spectrometer with Mg Kα excitation (1253.6 eV); carbon is used as the internal standard (C 1s = 284.6 eV). The diffuse reflectance spectra of the samples were measured in the range of 200–800 nm using a UV-vis spectrophotometer (UV-vis DRS, Hitachi U-3900, Japan) equipped with an integrating sphere attachment. Photoluminescence (PL) spectra of the different samples were investigated using a spectrophotometer (PL, Horiba Jobin Yvon Fluoromax 4C-L, France) with an excitation wavelength of 390 nm. To ensure the comparability of the PL spectra, the experimental parameters, including the excitation wavelength, slit width, and the amount of samples, were identical.

### Photocatalytic $H_2$ evolution measurements

Dye sensitization and stability test: a photocatalytic stability test was conducted to evaluate the performance of a catalyst under specific reaction conditions. The default reaction mixture comprised 2.5 mg of the catalyst, 5 mg of eosin-Y, 2 mL of triethanolamine (TEOA), and 18 mL of deionized water. Gas samples of 100 μL were extracted from the reaction system every hour to assess the reaction kinetics. For the stability test, each 4 hour interval was considered as one round, and the entire test consisted of 4 rounds. During the intermission periods, the reaction system was purged with nitrogen gas to refresh the gas composition, and 5 mg of eosin-Y was added to supplement the reaction mixture.

## Results and discussion

The catalysts including CoP, $Ni_2P$, CoNiP, and $CoNi_3P$, were synthesized following the procedure outlined in Scheme S1.† The precursor mixture, comprising Co and Ni salts along with $NaH_2PO_2$, underwent thermal treatment under a $N_2$ atmosphere at temperatures ranging from 220 °C to 300 °C for a duration of 1 hour. The X-ray diffraction (XRD) profiles, depicted in Fig. 1 and S1,† provide valuable insights regarding the crystalline phases present in the as-synthesized phosphides. The obtained CoP, CoNiP, and $Ni_2P$ materials were assigned to the *Pbnm* (62), $P\bar{6}2m$ (189), and $P\bar{6}2m$ (189) space groups, respectively. The XRD

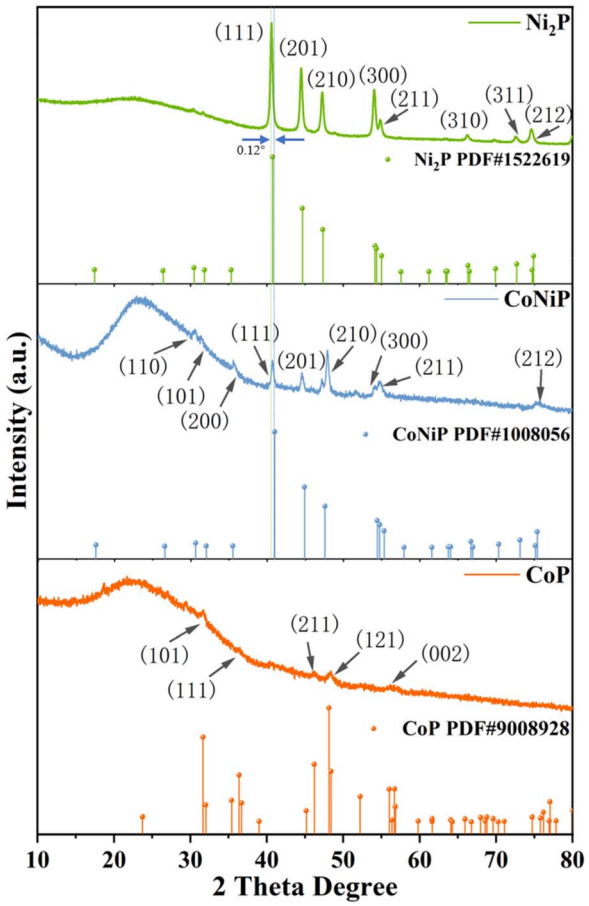


Fig. 1 Powder XRD patterns of as-prepared CoP, CoNiP and $Ni_2P$.

profiles of the $Ni_2P$ catalyst indicate the formation of a singular hexagonal phosphide phase, identified as the $Ni_2P$-type phase (PDF no. 1522619). Notably, the XRD pattern of $Ni_2P$ closely resembles those of CoNiP and $CoNi_3P$. Upon increasing the Co doping concentration, a subtle shift towards higher diffraction angles is observed in the positions of the XRD peaks. Particularly, the primary peak corresponding to the (111) crystal phase of CoNiP exhibits a positive shift of 0.12° compared to that of $Ni_2P$, confirming the successful incorporation of cobalt into the $Ni_2P$ lattice. Although the XRD pattern of $CoNi_3P$ exhibits the presence of some additional mixed phases, overall, it displays similar peak characteristics with CoNiP. Notably, the XRD pattern of CoP lacks distinct peaks, suggesting relatively lower crystallinity for this particular phosphide.

As depicted in the SEM image of Fig. S2,† the CoP exhibits a sintered elongated strip-like morphology, measuring approximately 200 nm in width. The ternary compounds (CoNiP and $CoNi_3P$) both display agglomerated states characterized by small particles undergoing sintering. The agglomerated structure of CoNiP reveals a considerable number of pores on its surface, with diameters ranging in the tens of nanometers, while the $CoNi_3P$ agglomerates exhibit fewer surface pores. The $Ni_2P$ exhibits an amorphous morphology with dispersed small particles ranging in diameter from tens to hundreds of nanometers.

The TEM testing results, as illustrated in Fig. 2 and S3,† reveal distinctive features of the synthesized materials. CoNiP exhibits a morphology structure resembling mesoporous materials, with pore sizes in the nanometer range. $Ni_2P$ forms thin sheet-like structures at the edges of the particles. High-resolution transmission electron microscopy (HRTEM) images demonstrate the well-defined lattice fringes in both CoNiP and $Ni_2P$, corresponding to the (111) and (200) crystal planes with lattice spacings of 0.22 nm and 0.25 nm, respectively. These observations are in agreement with the XRD patterns, indicating successful synthesis and good crystallinity of CoNiP and $Ni_2P$. In contrast, TEM results of CoP show the presence of wide pore structures. The HRTEM analysis indicates relatively poor crystallinity with less distinct lattice fringes. However, the faint lattice spacing of approximately 0.19 nm corresponding to the (121) crystal plane can still be observed, also consistent with the XRD results. The low crystallinity of CoP is due to the formation of CoP as an amorphous phase. It is further supported by the large wide peak observed in the range of 15–35°. $CoNi_3P$ particles also exhibit a porous structure, and two sets of lattice fringes consistent with $Ni_2P$ are visible, corresponding to the (111) and (200) crystal planes. However, no crystal planes consistent with CoP are identified, possibly due to the lower cobalt content and the absence of an independent phase formation.

Elemental mappings presented in Fig. S4† demonstrate the uniform distribution of Co, Ni, and P in all four samples. Energy-dispersive X-ray analysis (EDX) results (Fig. 2 and S5†)

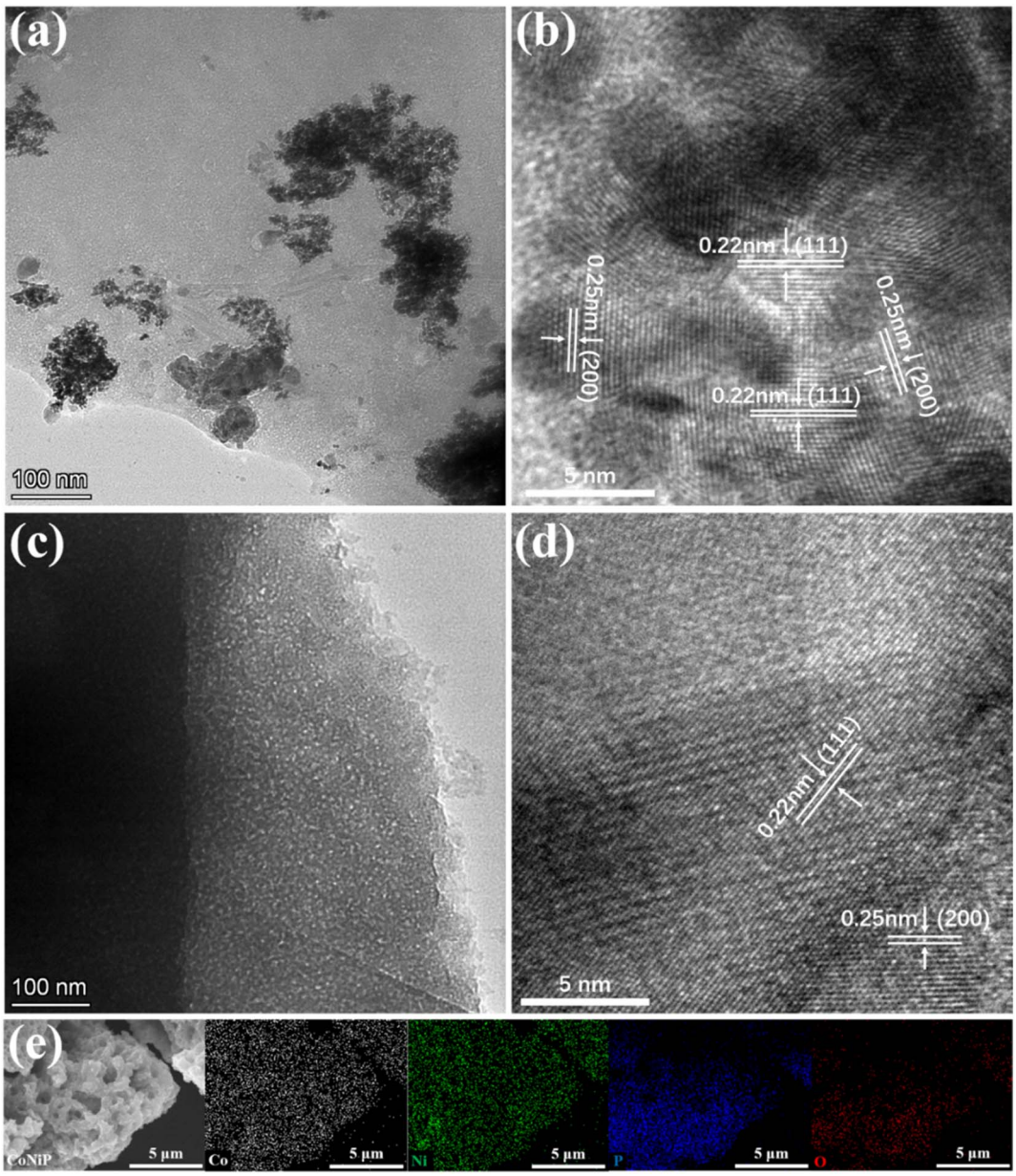


Fig. 2 The TEM and HRTEM images of (a and b) the CoNiP and (c and d) the $Ni_2P$ samples. (e) The elemental mapping images of CoNiP.

provide insights into the elemental composition of the samples. CoNiP exhibits similar Co and Ni contents, closely matching the theoretical elemental ratios. CoP and $Ni_2P$ show the respective Co and Ni content expected for their corresponding compounds. $CoNi_3P$ confirms the presence of both Co and Ni elements with a relative abundance ratio where Ni content is approximately 2–3 times higher than Co. However, the absolute contents of both elements in $CoNi_3P$ are relatively low. This may explain the incomplete crystalline phase formation and lower crystallinity observed in the $CoNi_3P$ sample.

X-ray photoelectron spectroscopy (XPS) was performed to investigate the energy levels of Co 2p, Ni 2p, P 2p, and O 1s in CoP, $Ni_2P$, CoNiP, and $CoNi_3P$ samples. As shown in Fig. 3 in the XPS spectrum of Co 2p, the characteristic peaks at 778.9 eV and 781.3 eV for CoP can be indexed to $Co^{\delta+}$ oxidation state in Co–P and the $Co^{2+}/Co^{3+}$,[53,57] respectively, and are in close proximity to the corresponding peaks in CoNiP. In the Ni 2p spectrum, the characteristic peaks at 852.6 eV and 856.3 eV for $Ni_2P$ correspond to Ni–P and Ni–O bonds,[58,59] respectively. The P 2p spectrum exhibits two main peaks, which correspond to the phosphate group and oxidized species of P.[60,61] In the O 1s spectrum, three main characteristic peaks are observed in each sample, with the peak near 531.5 eV attributed to oxygen deficiencies in the lattices.[62,63] The CoNiP sample shows a unique peak at 530.8 eV, possibly due to the coexistence of Co and Ni, which creates a distinct chemical environment around oxygen compared to the other two elements. The XPS spectrum of $CoNi_3P$ is displayed in Fig. S6.† In this spectrum, the signal intensities of Co 2p and Ni 2p are relatively weak, making it difficult to discern distinct characteristic peaks. This corresponds to the lower surface distribution of Co and Ni elements observed in the EDX analysis, which may be linked to the relatively low annealing temperature employed during the synthesis process. Besides, the O 1s and P 2p spectra exhibit similarities to those of $Ni_2P$.

Fig. 4 illustrates the photocatalytic hydrogen production activity of the prepared photocatalysts under different reaction conditions. A 2 mL solution of triethanolamine (TEOA) was employed as a sacrificial agent and electron donor to scavenge the photogenerated holes. Additionally, 5 mg of eosin-Y dye was used as a photosensitizer. Furthermore, 2.5 mg of the photocatalyst and 18 mL of deionized water were added as reactants. Fig. 4a compares the hydrogen production rates for CoP, $Ni_2P$, CoNiP, and $CoNi_3P$. Among them, CoNiP exhibits the highest activity, reaching 9.18 mmol $g^{-1}$ $h^{-1}$, which is approximately 40–50% higher than that of the binary phosphides CoP and $Ni_2P$ and significantly higher than that of $CoNi_3P$. This indicates that ternary phosphides possess superior photocatalytic activity compared to binary phosphides, and the ratio of the two metal elements also influences the activity.

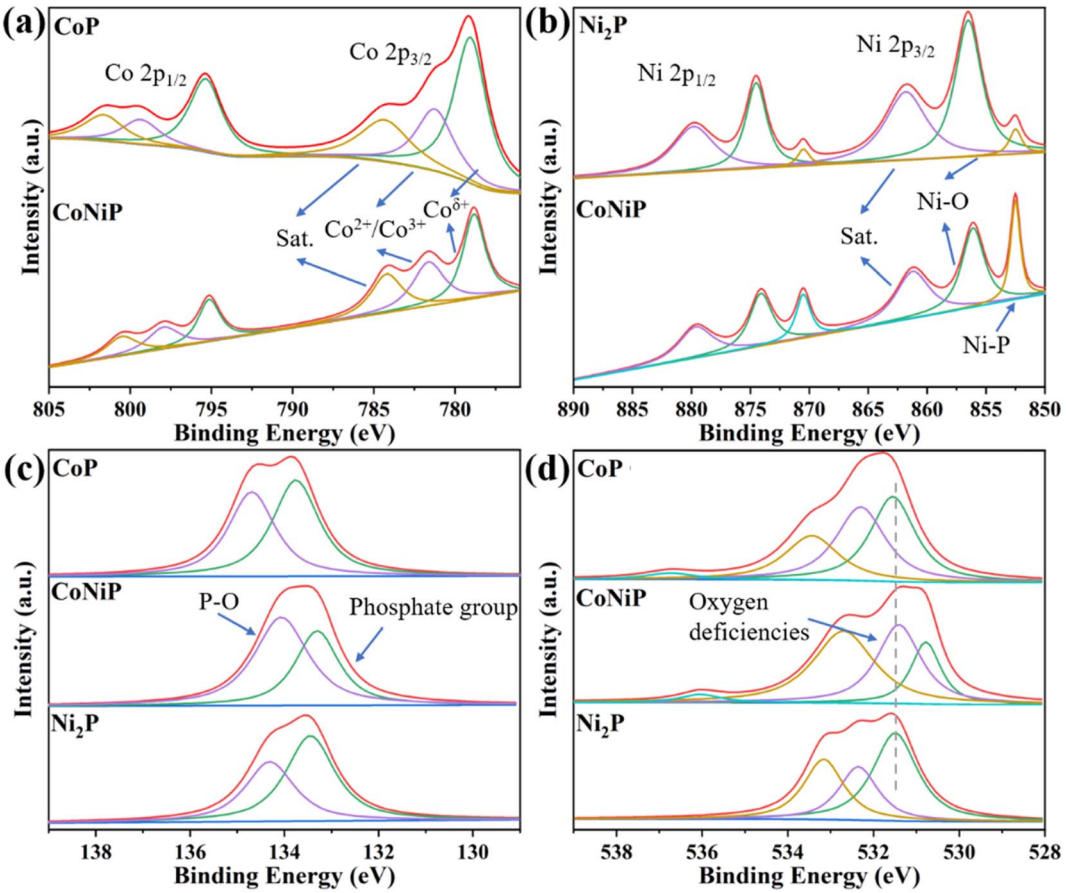


Fig. 3 The high-resolution XPS spectra of (a) Co 2p, (b) Ni 2p, (c) P 2p and (d) O 1s of CoP, CoNiP and $Ni_2P$ samples.

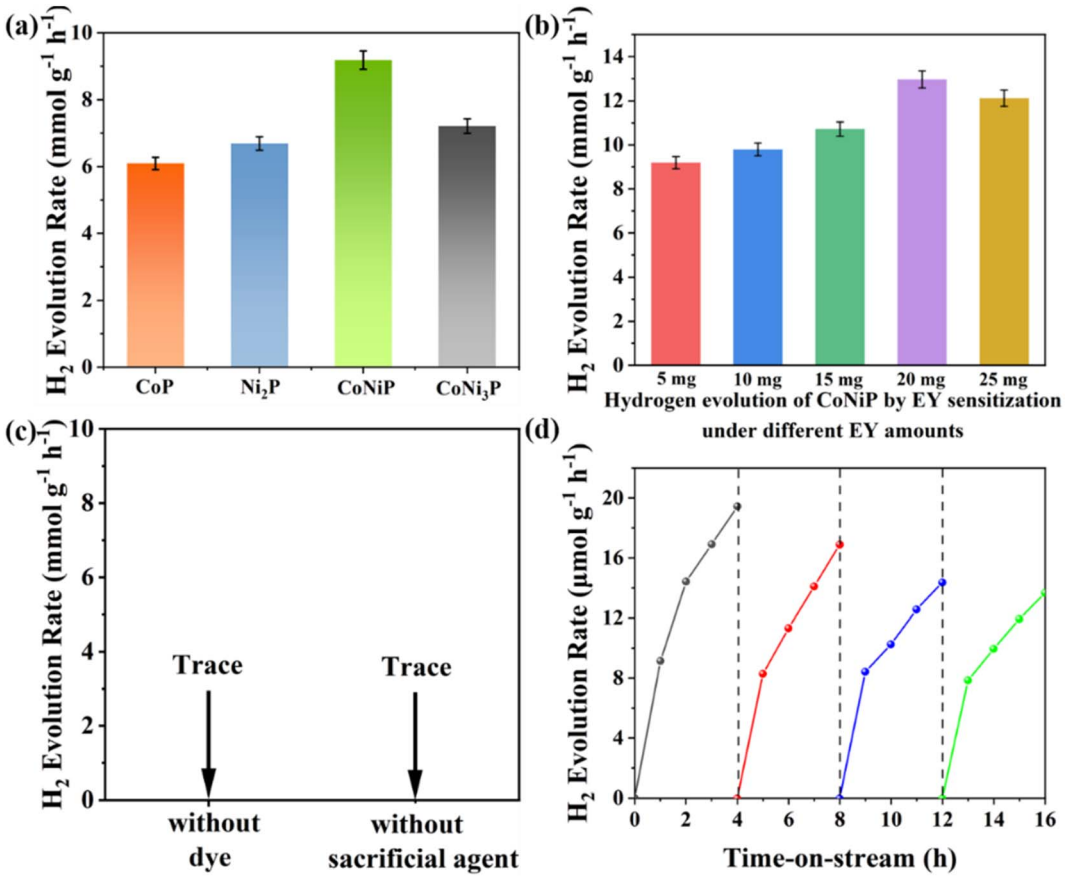


Fig. 4 (a) Photocatalytic $H_2$ evolution activities of CoP, $Ni_2P$, CoNiP and $CoNi_3P$ with using 2.5 mg of catalysts and 5 mg of eosin-Y. (b) The photocatalytic $H_2$ evolution efficiency of CoNiP with different amount of eosin-Y. (c) The controlled experiments for testing the roles of the dye and the sacrificial agent. (d) Stability test for the CoNiP sample of $H_2$ production (4 h for a round).

Further comparative experiments were conducted using only the CoNiP sample, with the eosin-Y dye concentration gradually increased from 5 mg to 25 mg (Fig. 4b), while keeping other conditions constant. It was found that when the eosin-Y concentration reached 20 mg (8 times the mass of the catalyst), the hydrogen production activity of CoNiP reached its maximum at 12.96 mmol $g^{-1}$ $h^{-1}$. This observation is consistent with the sensitization effect of the dye, which provides a sufficient number of electrons for the reaction, as described in the literature.[64] Additionally, the increased dye concentration promotes the adsorption of eosin-Y on the surface of CoNiP, thereby enhancing the hydrogen production rate.[38] However, after reaching an excessive dye concentration, the hydrogen production activity decreases due to the light-shielding effect.[65,66] This means that beyond the optimal dye concentration, eosin-Y remains in a free state and terminates reactions on some active sites, hindering the light absorption process of the reaction system. This activity of CoNiP is higher than most of the previously reported photocatalytic eosin-Y sensitized reaction systems, which is considerable (Table S1†).

Fig. 4c presents the results validating the necessity of various reaction components. It is observed that the hydrogen production activity approaches zero when either the dye or sacrificial agent is removed, indicating their indispensability during the reaction process. Finally, the long-term reaction stability of CoNiP was tested. Fig. 4d shows that after four cycles of four hour reaction periods, the hydrogen production activity decreased by approximately 30%. This may be attributed to the adsorption of the catalyst sample on the magnetic stirrer, affecting the effective interfacial area between the catalyst and the solution. It is also observed that the activity remains relatively stable during the first hour of each cycle without significant decline, possibly due to the replenishment of fresh dye in each cycle.

The XRD pattern of the CoNiP sample after stability test has been added in Fig. S7a.† It is notably that the CoNiP sample maintained a similar crystal structure before and after the stability test, with only slight weakening observed in some peaks and no peak shifting was detected. This indicates that the CoNiP catalyst exhibited considerable structural stability. The SEM and HRTEM images have been added in Fig. S7b and c.† The comparison with the corresponding images before the reaction reveals valuable insights into the morphological changes of the CoNiP catalyst during the stability test. The observed slight agglomeration and reduction in surface holes indicate that the CoNiP catalyst undergoes some minor changes of morphology during the stability test. However, despite these changes, the TEM image still shows the presence of the crystal phase of (111) through the identification of the crystal instance

at approximately 0.22 nm. Thus, the CoNiP catalyst maintains a stable crystal structure throughout the stability test.

The solid UV-vis DRS (diffuse reflectance spectrum) pattern is shown in Fig. S8a.† The observed patterns indicate that the relative absorbance of all samples across various wavelength is similar, but CoP exhibited significantly higher absolute absorbance compared to the other three samples. While CoNiP may not exhibit the highest absorbance among the four samples, it is essential to note that absorbance alone is not the decisive factor in the activity of photocatalytic hydrogen evolution.[67,68] Besides, all samples display relatively lower absorbance in the short wavelength range and relatively higher absorbance in the long wavelength range. In the vicinity of 350 nm, a small trough is observed with a slight decrease in absorbance. Similarly, near the 600 nm range, a shallow trough is evident, with CoP showing a relatively more obscure trough compared to the other samples.

The photoluminescence (PL) spectrum is exhibited in Fig. S8b.† It indicates that $CoNi_3P$ exhibited the lowest PL intensity among the four samples, suggesting a more prominent suppression of the recombination of electrons and excited state of EY compare to the other three samples.[69] Meanwhile, the CoP and CoNiP have higher PL intensity. However, the PL intensity is also not the sole decisive factor in determining the photocatalytic performance. Various other factors, such as the crystallinity, surface properties, catalytic sites can play important roles in influencing the photocatalytic activity.

Fig. 5 presents the characterization of the four photocatalyst samples through electrocatalytic testing. Fig. 5a displays cyclic voltammograms (CV) curves without distinct cathodic and anodic peaks. In the electrocatalytic testing, the electrode and electrolyte are identical, so the current density is solely related to the electron transfer rate of the electrode material.[70,71] It can be observed that the CoNiP sample exhibits a higher current density compared to the other three samples, indicating its ability to facilitate charge carrier transfer in the catalyst. Additionally, the specific capacitance performance was measured in a three-electrode system (Fig. S9†). The current density curve of CoNiP encloses a larger area than the other samples, suggesting its superior electron acceptance capability. Electrochemical impedance spectroscopy (EIS) was conducted, and the corresponding Nyquist plots for different samples are presented in Fig. 5b. It can be observed that the radius of the CoNiP sample's curve is the smallest among all the samples and significantly smaller than that of the binary

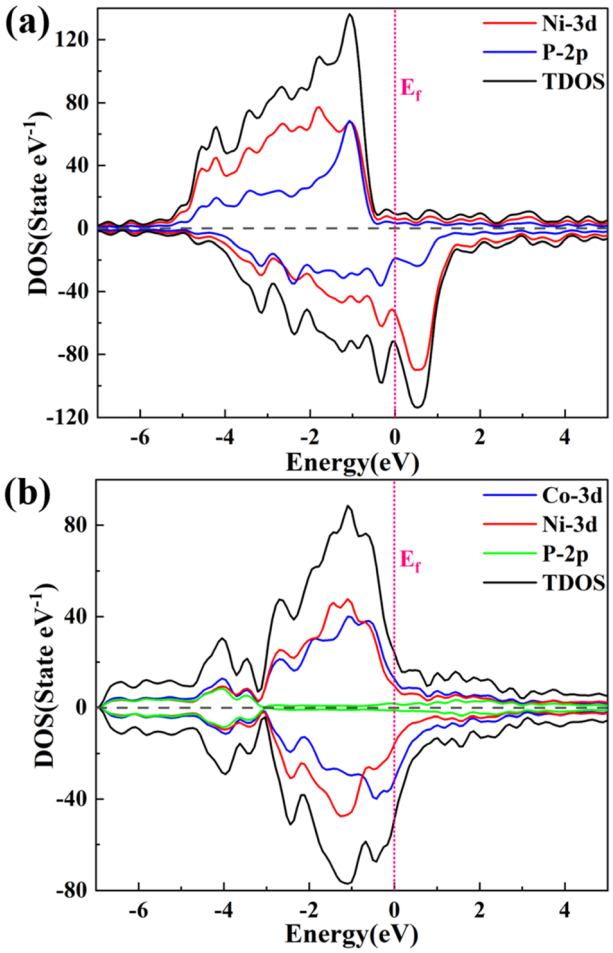


Fig. 6 Total electron density of states (DOS) of (a) $Ni_2P$ and (b) CoNiP, which projected on Co, Ni and P atoms. The Fermi level is set as zero.

phosphides. This result further confirms the conclusions drawn from the CV curves and indicates that CoNiP possesses a higher efficient charge carrier capacity.[72,73] Fig. 5c shows the polarization curves. It is evident that CoNiP exhibits a more negative current density within a similar potential range, indicating a stronger promoting effect on the $H_2$ evolution reaction.[54] These results are reasonable due to the higher electron conductivity and lower electrocatalytic overpotential of phosphides. Meanwhile, the considerable electrocatalytic properties of CoNiP is also corresponding to its $H_2$ evolution rate.

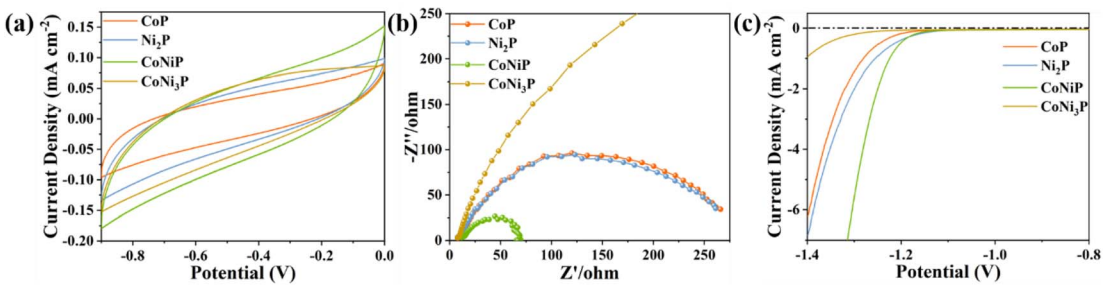


Fig. 5 The (a) cyclic voltammograms, (b) EIS Nyquist plots and (c) polarization curves of CoP, CoNiP, $CoNi_3P$ and $Ni_2P$ samples.

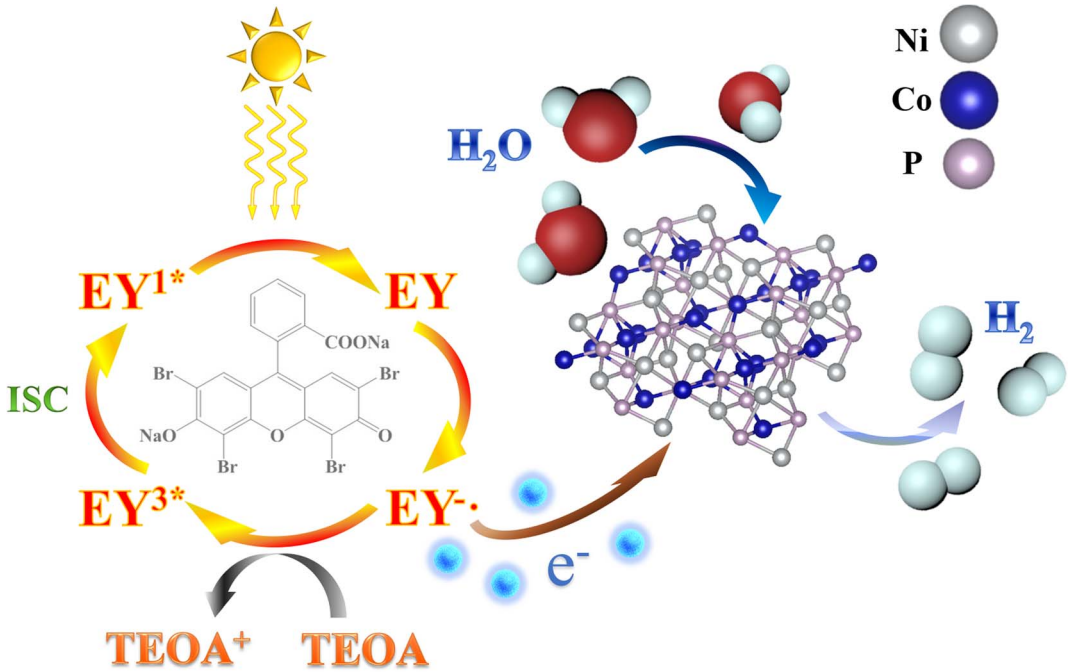


Scheme 1 The proposed photocatalytic hydrogen production mechanism over the eosin-Y sensitized CoNiP under visible light irradiation.

Fig. 6 presents the DFT calculation results of the calculated partial density of states (PDOS) on the (111) crystal plane for the CoNiP and $Ni_2P$ samples. As shown, the metallic nature of the samples and the presence of free electrons. The density of states near the Fermi level is primarily composed of Ni 3d or Ni 3d and Co 3d, confirming the excellent conductivity of the phosphides.[74–76] Additionally, the average d-band center positions were calculated for $Ni_2P$ and CoNiP, resulting in −1.296 eV and −1.336 eV, respectively. Thus, the average d-band center of CoNiP is more negative than that of $Ni_2P$, which is attributed to the introduction of Co, leading to a change in the density of states near the Fermi level. According to the d-band theory, the negative shift of the d-band center weakens the adsorption of the catalyst on $H_2$ molecules, facilitating the evolution of $H_2$ in the reaction. This provides an explanation for the more superior hydrogen evolution performance of CoNiP than those of the binary phosphide.[54,77,78]

The proposed mechanism for photocatalytic $H_2$ production facilitated by the eosin-Y sensitized CoNiP system is illustrated in Scheme 1. Initially, the molecules absorb photons from the visible light spectrum, leading to the formation of the single excited state $EY^{1*}$. Subsequently, an intersystem crossing (ISC) occurs, resulting in the generation of a more stable triplet excited state, $EY^{3*}$. In the presence of TEOA as an electron donor, $EY^{3*}$ is reduced to $EY^{-\cdot}$, an ion with a pronounced reduction capacity.[64] The electrons originating from $EY^{-\cdot}$ are efficiently transferred to the surfaces of CoNiP due to its metallic-like properties. Consequently, a reduction reaction takes place at these sites, ultimately yielding $H_2$. Simultaneously, the eosin-Y dye molecules, having undergone reduction, revert to their ground state. The CoNiP structure exhibits remarkable electron transfer and acceptor behavior, thereby restricting the recombination of photo-generated charges and holes.[64] Consequently, the efficiency of photocatalytic hydrogen production is significantly enhanced.

## Conclusions

In conclusion, we have synthesized a series of cobalt–nickel phosphides, including CoP and $Ni_2P$ as binary phosphides, as well as CoNiP and $CoNi_3P$ as ternary phosphides, for dye-sensitized photocatalytic hydrogen evolution. When the optimal ratio of dye to catalyst mass was used (20 mg : 2.5 mg), CoNiP achieved a hydrogen evolution efficiency of 12.96 mmol $g^{-1}$ $h^{-1}$, which is satisfactory. This is primarily due to the excellent conductivity of the phosphides, attributed to their metallic nature and the presence of free electrons, which significantly enhances the electron transfer rate between the catalyst and photosensitizer and promotes the separation of electron–hole pairs. Furthermore, experimental and DFT calculations have shown that the introduction of Co in $Ni_2P$ alters the density of states near the Fermi level, resulting in a more negative average d-band center position for the ternary phosphide CoNiP compared to the binary phosphide with a single metal component. This negative shift weakens the adsorption of $H_2$ molecules, thereby effectively improving the hydrogen evolution activity of the catalyst. This work provides valuable insights for the development of low-cost, high-performance ternary phosphide photocatalysts as alternatives to noble metals.

## Conflicts of interest

There are no conflicts to declare.

## Acknowledgements

The authors acknowledge the financial support from the Guangdong Academy of Sciences special fund project (Research on the key technology and its application of semiconductor integrated circuit, ref. 1222280008006), Postdoctoral special funds (ref. 1223280002) and the Hong Kong Polytechnic University research project (Ergonomic leggings with twisted actuation yarns for improving compression therapy, ref. P0037701) and the Postdoc Matching Fund Scheme (ref. 1-W265).

## References

1 S. Tian, C. Zhang, D. Huang, R. Wang, G. Zeng, M. Yan, W. Xiong, C. Zhou, M. Cheng, W. Xue, Y. Yang and W. Wang, *Chem. Eng. J.*, 2020, **389**, 123423.
2 B. Li, C. Lai, M. Zhang, G. Zeng, S. Liu, D. Huang, L. Qin, X. Liu, H. Yi, F. Xu, N. An and L. Chen, *Adv. Energy Mater.*, 2020, **10**, 2000177.
3 H. Luo, Z. Zeng, G. Zeng, C. Zhang, R. Xiao, D. Huang, C. Lai, M. Cheng, W. Wang, W. Xiong, Y. Yang, L. Qin, C. Zhou, H. Wang, Y. Zhou and S. Tian, *Chem. Eng. J.*, 2020, **383**, 123196.
4 Y. Liu, D. Huang, M. Cheng, Z. Liu, C. Lai, C. Zhang, C. Zhou, W. Xiong, L. Qin, B. Shao and Q. Liang, *Coord. Chem. Rev.*, 2020, **409**, 213220.
5 Z. Cheng, W. Qi, C. H. Pang, T. Thomas, T. Wu, S. Liu and M. Yang, *Adv. Funct. Mater.*, 2021, 2100553.
6 A. Fujishima and K. Honda, *Nature*, 1972, **238**, 37–38.
7 Y. Zhou, W. Wang, C. Zhang, D. Huang, C. Lai, M. Cheng, L. Qin, Y. Yang, C. Zhou, B. Li, H. Luo and D. He, *Adv. Colloid Interface Sci.*, 2020, **279**, 102144.
8 J. Schneider, M. Matsuoka, M. Takeuchi, J. Zhang, Y. Horiuchi, M. Anpo and D. W. Bahnemann, *Chem. Rev.*, 2014, **114**, 9919–9986.
9 Y. H. Ng, R. Shen, D. Ren, Y. Ding, Y. Guan, P. Zhang and X. Li, *Sci. China Mater.*, 2020, **63**, 2153–2188.
10 Z. Fan, X. Guo, M. Yang and Z. Jin, *Chin. J. Catal.*, 2022, **43**, 2708–2719.
11 G. Liao, B. Fang and C. Li, *Chem Catal.*, 2023, **3**, 100671.
12 K. Qi, B. Cheng, J. Yu and W. Ho, *J. Alloys Compd.*, 2017, **727**, 792–820.
13 Y. Yang, X. Li, C. Zhou, W. Xiong, G. Zeng, D. Huang, C. Zhang, W. Wang, B. Song, X. Tang, X. Li and H. Guo, *Water Res.*, 2020, **184**, 116200.
14 X. Li, Z. Zeng, G. Zeng, D. Wang, R. Xiao, Y. Wang, C. Zhou, H. Yi, S. Ye, Y. Yang and W. Xiong, *J. Colloid Interface Sci.*, 2020, **561**, 501–511.
15 G. Liao, X. Tao and B. Fang, *Matter*, 2022, **5**, 377–389.
16 C. Li, G. Liao and B. Fang, *Chem Catal.*, 2022, **2**, 221–241.
17 G. Liao, C. Li, S.-Y. Liu, B. Fang and H. Yang, *Phys. Rep.*, 2022, **983**, 1–41.
18 G. Liao, C. Li, S.-Y. Liu, B. Fang and H. Yang, *Trends Chem.*, 2022, **4**, 111–127.
19 R. Liang, Y. Wang, C. Qin, X. Chen, Z. Ye and L. Zhu, *Langmuir*, 2021, **37**, 3321–3330.
20 E. Ossama, K. Sooyeon, F. Mamoru and M. Tetsuro, *Nano Energy*, 2017, **35**, 2211–2855.
21 A. Meng, L. Zhang, B. Cheng and J. Yu, *Adv. Mater.*, 2019, **31**, 1807660.
22 N. Zhang, L. Wen, J. Yan and Y. Liu, *Chem. Pap.*, 2020, **74**, 389–406.
23 J. Xu, Y. Li and S. Peng, *Int. J. Hydrogen Energy*, 2015, **40**, 353–362.
24 S. Min and G. Lu, *J. Phys. Chem. C*, 2012, **116**, 19644–19652.
25 S. Peng, X. Huang, Y. Cao, J. Zuo, Y. Huang, J. Xu and Y. Li, *Appl. Surf. Sci.*, 2022, **584**, 152610.
26 J. Ran, J. Zhang, J. Yu, M. Jaroniec and S. Z. Qiao, *Chem. Soc. Rev.*, 2014, **43**, 7787–7812.
27 Y. Yang, C. Zhou, W. Wang, W. Xiong, G. Zeng, D. Huang, C. Zhang, B. Song, W. Xue, X. Li, Z. Wang, D. He, H. Luo and Z. Ouyang, *Chem. Eng. J.*, 2021, **405**, 126547.
28 J. Liu, Y. Li, X. Zhou, H. Jiang, H. G. Yang and C. Li, *J. Mater. Chem. A*, 2020, **8**, 17–26.
29 S. Meng, P. An, L. Chen, S. Sun, Z. Xie, M. Chen and D. Jiang, *J. Colloid Interface Sci.*, 2021, **585**, 108–117.
30 R. Camposeco, M. Hinojosa-Reyes and R. Zanella, *Int. J. Hydrogen Energy*, 2021, **46**, 26074–26086.
31 W. A. Qureshi, X. Hong, X. He, Q. Liu, D. Xu, C. Maouche, Z. Sun and J. Yang, *Chemosphere*, 2022, **291**, 132987.
32 N. Güy, *Appl. Surf. Sci.*, 2020, **522**, 146442.
33 T. Hisatomi, J. Kubota and K. Domen, *Chem. Soc. Rev.*, 2014, **43**, 7520–7535.
34 S. Chen, J. Liao, Z. Zhou, S. Yang, Q. Gao, X. Cai, F. Peng, Y. Fang and S. Zhang, *Appl. Catal., B*, 2021, **291**, 120139.
35 Y. Tan, Z. Shu, J. Zhou, T. Li, W. Wang and Z. Zhao, *Appl. Catal., B*, 2018, **230**, 260–268.
36 C. Yang, J. Qin, Z. Xue, M. Ma, X. Zhang and R. Liu, *Nano Energy*, 2017, **41**, 1–9.
37 S. Zijun, C. Huanlin, Z. Lei, L. Dapeng and D. Pingwu, *J. Mater. Chem. A*, 2016, **4**, 13289–13295.
38 Z. Cheng, A. Saad, S. Adimi, H. Guo, S. Liu, T. Thomas and M. Yang, *Mater. Adv.*, 2020, **1**, 1161–1167.
39 H. Xu, S. Li, L. Ge, C. Han, Y. Gao and D. Dai, *Int. J. Hydrogen Energy*, 2017, **42**, 22877–22886.
40 L. Xie, J.-G. Hao, H.-Q. Chen, Z.-X. Li, S.-Y. Ge, Y. Mi, K. Yang and K.-Q. Lu, *Catal. Commun.*, 2022, **162**, 106371.
41 L. Mao, X.-Y. Cai and M.-S. Zhu, *Rare Met.*, 2021, **40**, 1067–1076.
42 Z. Jin, H. Li and J. Li, *Chin. J. Catal.*, 2022, **43**, 303–315.
43 R. M. Irfan, M. H. Tahir, S. Iqbal, M. Nadeem, T. Bashir, M. Maqsood, J. Zhao and L. Gao, *J. Mater. Chem. C*, 2021, **9**, 3145–3154.
44 F. Yang, D. Liu, Y. Li, L. Cheng and J. Ye, *Chem. Eng. J.*, 2020, **399**, 125794.
45 S. Iqbal, *Appl. Catal., B*, 2020, **274**, 119097.
46 X. Yan and Z. Jin, *Chem. Eng. J.*, 2021, **420**, 127682.
47 H. Zhao, L. Jian, M. Gong, M. Jing, H. Li, Q. Mao, T. Lu, Y. Guo, R. Ji, W. Chi, Y. Dong and Y. Zhu, *Small Struct.*, 2022, **3**, 2100229.
48 Y. Pan, K. Sun, S. Liu, X. Cao, K. Wu, W.-C. Cheong, Z. Chen, Y. Wang, Y. Li, Y. Liu, D. Wang, Q. Peng, C. Chen and Y. Li, *J. Am. Chem. Soc.*, 2018, **140**, 2610–2618.

49 S. He, S. He, F. Gao, X. Bo, Q. Wang, X. Chen, J. Duan and C. Zhao, *Appl. Surf. Sci.*, 2018, **457**, 933–941.
50 S. H. Li, N. Zhang, X. Xie, R. Luque and Y. J. Xu, *Angew. Chem., Int. Ed.*, 2018, **57**, 13082–13085.
51 J. Hu, X. Zhao, W. Chen, S. Zheng and Z. Chen, *Sol. RRL*, 2020, **4**, 1900360.
52 E. J. Popczun, J. R. McKone, C. G. Read, A. J. Biacchi, A. M. Wiltrout, N. S. Lewis and R. E. Schaak, *J. Am. Chem. Soc.*, 2013, **135**, 9267–9270.
53 S. Peng, Y. Cao, F. Zhou, Z. Xu and Y. Li, *Appl. Surf. Sci.*, 2019, **487**, 315–321.
54 J. Li, M. Yan, X. Zhou, Z.-Q. Huang, Z. Xia, C.-R. Chang, Y. Ma and Y. Qu, *Adv. Funct. Mater.*, 2016, **26**, 6785–6796.
55 X. Yue, S. Yi, R. Wang, Z. Zhang and S. Qiu, *Small*, 2017, **13**, 1603301.
56 P. Wang, S. Zhan, H. Wang, Y. Xia, Q. Hou, Q. Zhou, Y. Li and R. R. Kumar, *Appl. Catal., B*, 2018, **230**, 210–219.
57 Z. Cheng, A. Saad, H. Guo, C. Wang, S. Liu, T. Thomas and M. Yang, *J. Alloys Compd.*, 2020, **838**, 155375.
58 H.-W. Man, C.-S. Tsang, M. M.-J. Li, J. Mo, B. Huang, L. Y. S. Lee, Y. Leung, K.-Y. Wong and S. C. E. Tsang, *Appl. Catal., B*, 2019, **242**, 186–193.
59 Z. Huang, Z. Chen, Z. Chen, C. Lv, H. Meng and C. Zhang, *ACS Nano*, 2014, **8**, 8121–8129.
60 A. Indra, A. Acharjya, P. W. Menezes, C. Merschjann, D. Hollmann, M. Schwarze, M. Aktas, A. Friedrich, S. Lochbrunner, A. Thomas and M. Driess, *Angew. Chem., Int. Ed.*, 2017, **56**, 1653–1657.
61 K.-Q. Lu, M.-Y. Qi, Z.-R. Tang and Y.-J. Xu, *Langmuir*, 2019, **35**, 11056–11065.
62 S. Deng, R. Chen, G. Li, M. Zhang, Z. Xia, M. Wong and H.-S. Kwok, *IEEE Electron Device Lett.*, 2018, **39**, 975–978.
63 M. G. Yun, C. H. Ahn, S. W. Cho, S. H. Kim, Y. K. Kim and H. K. Cho, *ACS Appl. Mater. Interfaces*, 2015, **7**, 6118–6124.
64 D. Liu, Z. Jin and Y. Bi, *Catal. Sci. Technol.*, 2017, **7**, 4478–4488.
65 X. Hao, Z. Jin and G. Lu, *Chem. Lett.*, 2016, **45**, 116–118.
66 J. Moser and M. Grätzel, *J. Am. Chem. Soc.*, 1984, **106**, 6557–6564.
67 Y. Cao, H. Gou, P. Zhu and Z. Jin, *Chin. J. Struct. Chem.*, 2022, **41**, 2206079–2206085.
68 T. Yan, X. Zhang, H. Liu and Z. Jin, *Chin. J. Struct. Chem.*, 2022, **41**, 2201047–2201053.
69 S. Liu, X. Meng, S. Adimi, H. Guo, W. Qi, J. P. Attfield and M. Yang, *Chem. Eng. J.*, 2021, **408**, 127307.
70 B. Weng, Q. Quan and Y. Xu, *J. Mater. Chem. A*, 2016, **4**, 18366–18377.
71 C. Han, Z. Chen, N. Zhang, J. C. Colmenares and Y. J. Xu, *Adv. Funct. Mater.*, 2015, **25**, 221–229.
72 B. Weng and Y. Xu, *ACS Appl. Mater. Interfaces*, 2015, **7**, 27948–27958.
73 N. Zhang and Y. Xu, *Chem. Mater.*, 2013, **25**, 1979–1988.
74 Z. Chen, J. Wang and C. Li, *J. Alloys Compd.*, 2013, **575**, 137–144.
75 Y. Gu, S. Chen, J. Ren, Y. A. Jia, C. C. Chen, S. Komarneni, D. Yang and X. Yao, *ACS Nano*, 2018, **12**, 245–253.
76 Y. Yuan, L. Yang, B. He, E. Pervaiz, Z. Shao and M. Yang, *Nanoscale*, 2017, **9**, 6259–6263.
77 N. Yao, P. Li, Z. Zhou, Y. Zhao, G. Cheng, S. Chen and W. Luo, *Adv. Energy Mater.*, 2019, **9**, 1902449.
78 Z. Chen, Y. Song, J. Cai, X. Zheng, D. Han, Y. Wu, Y. Zang, S. Niu, Y. Liu, J. Zhu, X. Liu and G. Wang, *Angew. Chem., Int. Ed.*, 2018, **57**, 5076–5080.